Supplementary Materials: Electronic Annex

Surficial weathering of iron sulfide mine tailings under semi-arid climate

Sarah M. Hayes, Robert A. Root, Nicolas Perdrial, Raina Maier and Jon Chorover*

Department of Soil, Water and Environmental Science,

University of Arizona, Tucson, AZ 85721

Submitted to:

Geochimica et Cosmochimica Acta

* Address correspondence to Jon Chorover, Department of Soil, Water and Environmental Science, University of Arizona, 1177 E 4th St, Shantz 429, Tucson, AZ 85721
Telephone: +1 520-626-5635, Fax: 520-626-1647, E-mail: chorover@cals.arizona.edu

Pages: 16

Sequential Extraction Procedure

The SSE procedure was modified after Dold (2003) and Neaman et al. (2004) and performed as follows:1) deionized water (H_2O), 1 h at room temperature (25^oC, RT), targeting soluble efflorescent salts, e.g. gypsum; 2) 1 M ammonium nitrate, 2h at RT with a DI wash targeting easily exchangeable and plant/bioavailable ions and metals; 3) 1M ammonium acetate with pH adjusted to 4.5 with acetic acid and a DI wash, targeting non-specifically sorbed ions and acid soluble carbonates; 4) 1.0M ammonium phosphate, 24 hr with pH adjusted to 5.0 with acetic acid and a DI wash, targeting specifically sorbed ligands, e.g. inner sphere As complexed on ferric (hyr)oxide surface sites; 5) 0.1 M ascorbic acid plus 0.2 M ammonium oxalate, 2 h in the dark at pH 3.0 adjusted with oxalic acid with an acetic acid wash to dissolve precipitated oxalates , targeting poorly crystalline Al, Mn, and Fe (oxyhydr)oxides, including ferrihydrite and schwertmannite; and 6) 1 M citrate-dithionite-bicarbonate with an acetic acid wash, targeting reducible crystalline Al, Mn, and Fe (oxyhydr)oxides and (hydroxy)sulfates, including goethite and jarosite. Sediment aliquots were sequentially treated with each extractant solution (solid: solution = 1:40 by mass), the suspensions were centrifuged (25 min at 11 000 g), and the supernatant was decanted and filtered (0.45 μm nylon membrane filters). Between extraction steps, sediments were washed with 10 mL of deionized water (18.2 MΩ-cm), centrifuged, and the supernatant decanted. The filtrate from each extraction step was analyzed by ICP-MS. After these extractions were performed, the residual solids underwent elemental analysis after dissolution using lithium metaborate/tetraborate fusion with inductively coupled plasma optical emission mass spectrometry (ICP-OES). Averages are reported from extractions run in triplicate and compared to total

concentrations from the total digestion of a split sample described above. Samples were sacrificed at each step in the SSE and frozen prior for analysis by x-ray diffraction (XRD) and Fe- XANES analysis.

Petrographic Analysis

A split subsample of the <2 mm fraction was air dried under 5% H2/95% N2 and embedded using degassed ultra-clean low-temperature set epoxy (EpoTek 301™). Uniform 30 μm thin sections were cut and ground under an anaerobic environment (Spectrum Petrographics Vancouver, WA). The epoxy-impregnated 30 μm thin sections were bonded to arsenic free quartz slides using cyanoacrylate adhesive (Superglue™). Each thin section was examined with a reflected and cross polarized light microscope. Distinct textural zones and grains of quartz and oxidized v. sulfide grains with and without oxidized rinds were identified in terms of color and morphology (reflected light). Petrographic analysis would have been complicated due to fine grain-size and poorly crystalline nature of the tailings. Electron and synchrotron microprobe (EMPA and u-XRF, respectively) were utilized to further characterize the petrology and elemental associations of the samples. For EMPA, thin sections were carbon coated and analyzed at the Lunar and Planetary Laboratory at the University of Arizona (CAMECA SX100 with WDS), operated at a 15 keV and a beam current of 9.77 nA and a spot size of about 2 μm. Synchrotron x-ray micro fluorescence (μ-XRF) was performed at SSRL. Thin sections further interrogated by micro-focused XRF maps and XAS spectra at the Stanford Synchrotron Radiation Lightsource (SSRL) at 13000 eV and 13050 eV (to differentiate As K-α from Pb L-III) using Si(111) crystal and a Vortex single element

detector (SII Nano Technology, Northridge, CA) at beam lines 10-2 and 2-3 with a spot size of 30 μm and 2 μm, respectively.

SSE Fe-XANES Analysis

The SSE-XANES spectra can be used to constrain model fits for complex and heterogeneous natural samples by uncovering phases that would otherwise be overlain and convoluted, making them potentially more difficult to identify. SSE-XANES, as used here without weight adjusted amplitude correction can be used to constrain and identify possible phases, but not the fractional component, used in linear combination fits after targeted phases are dissolved. The method is similar to differential x-ray diffraction can elucidate mineral Bragg reflections lost or gained as a function of reaction in a series of sequential extractions (Dold, 2003; Caraballo et al., 2009). Splits from the IK composite SSE series were examined before and after each SSE by Fe XANES. Examination of the residual revealed isolated phases as well as phases extracted and were used to guide the selection of component models in fits for the pit samples..

Geochemical Modeling

Equilibrium activity diagrams depicting theoretical stability relations among solid phases and aqueous species were computed with the ACT2 program in GWB. Precipitation of the thermodynamically stable phases of hematite, goethite, and magnetite was suppressed in the model to show the metastable phases of ferrihydrite, schwertmannite, and jarosite. Modified database from the LLNL dataset

thermo.com.V8.R6+ (Delany and Lundeen, 1990). There are disagreements in the literature on ferrihydrite structure (Waychunas et al., 1993; Zhao et al., 1994; Manceau and Gates, 1997; Janney et al., 2000; Michel et al., 2007), and solubility products (e.g. log K_{sp} = 3.0 to 5.66; Delany and Lundeen, 1990; Majzlan et al., 2004).

SM Table 1: Reference minerals used in NEXAFS and XANES linear combination fits

Mineral	Formula	Source[a]	Lot/ locality	Published
ankerite[b]	$Ca(Fe_{0.68},Mg_{0.32})(CO_3)_2$	Natural	Pulaski Co., AR, USA	This study
chlorite	$(Mg, Fe)_5Al(Si_3Al)O_{10}(OH)_8$	CMR	CCa-2	O'Day et al., 2004
ferrihydrite	$Fe_2O_3 \cdot 2FeOOH \cdot 2.6H_2O$ or $Fe_2O_3 \cdot nH_2O$	Syn.	na	Gao et al., 2013
gypsum	$CaSO_4 \cdot 2H_2O$	Wards	Alberta, Canada	This study
plumbojarosite	$PbFe_6(SO_4)_4(OH)_{12}$	UAM	5751	Hayes et al., 2009
pyrite	FeS_2	Natural	unknown	O'Day et al., 2004
schwertmannite	$Fe_8O_8(OH)_6(SO_4)$	Syn.	na	Bigham et al., 1990
melanterite	$Fe(SO_4) \cdot 7H_2O$	EM	unknown	This study

[a] Source identifications are CMR – clay minerals repository, Wards – Wards Scientific Inc., UAM – University of Arizona Mineral Museum, Syn. – Synthetic, and EM – Excalibur Mineral.

[b] Verified with XRD (PDF# 01-083-1531), ferrous content not quantified, stoichiometry from reference mineral.

SM Table 2: Minerals and formula for sulfur reference library, spectra in SM Fig. 3

<u>Sulfates</u>	
gypsum	$CaSO_4 \cdot 2H_2O$
Iron (II) sulfate	$FeSO_4$
goslarite	$ZnSO_4 \cdot 7H_2O$
plumbojarosite	$Pb(Fe_3(SO_4)_2(OH)_6)_2$
sodium sulfate	Na_2SO_4
thaumasite	$Ca_3\,SO_4\,Si(OH)_6\,CO_3 \cdot 12\,H_2O$
iron (III) sulfate	$Fe_2(SO_4)_3$
mercury sulfate	$HgSO_4$
anglesite	$PbSO_4$
<u>Intermediates</u>	
sodium sulfite	Na_2SO_3
potassium sulfite	K_2SO_3
methionine	$C_5H_{11}NO_2S$
cysteine	$C_3H_7NO_2S$
potassium tetrathionate	$K_2S_4O_6$
sodium thiosulfate	$Na_2S_2O_3$
potassium thiosulfate	$K_2S_2O_3$
elemental sulfur	S
<u>Sulfides</u>	
pyrite	FeS_2
marcasite	FeS_2
Iron (II) sulfide	FeS
troilite	FeS
arsenopyrite	FeAsS
sphalerite	ZnS
cinnabar	HgS
metacinnabar	HgS
realgar	α-As_4S_4
orpiment	As_2S_3

SM Table 3: Minerals and formula for iron reference library, spectra in SM Fig.4

Carboante/Sulfide (ferrous)

1. Siderite	$Fe^{II}CO_3$
2. Ankerite	$Ca(Fe^{II},Mg)(CO_3)_2$
3. Pyrite[a]	$Fe^{II}S_2$
4. Arsenopyrite[b]	$Fe^{II}AsS$

Hydroxide (ferric/mixed)

5. Ferrihydrite	$Fe^{III}(OH)_3$ - shorthand
	$5Fe_2O_3 \cdot 9H_2O$ - IMA '73
	$Fe_{10}O_{14}(OH)_2$ - Michel et al. '10
6. Goethite[a]	α-$Fe^{III}OOH$
7. Maghemite	γ-$Fe_2^{III}O_3$
8. Hematite[a]	α-$Fe_2^{III}O_3$
9. Magnetite[a]	$Fe^{II}Fe_2^{III}O_4$

Sulfate (ferrous/ferric/mixed)

10. Melanterite	$Fe^{II}SO_4$
11. Plumbojarosite[c]	$Pb^{II}Fe^{III}_6(SO_4)_4(OH)_{12}$
12. Jarosite	$KFe^{III}_3(SO_4)_2(OH)_6$
13. Schwerrtmannite	$Fe^{III}_{16}O_{16}(OH)_{12}(SO_4)_2$
14. Greenrust II SO_4[b]	$Fe^{II}_4Fe^{III}_2(OH)_2(SO_4) \cdot 6H_2O$

Arsenate/Phosphate/Silicate (ferrous/mixed)

15. Scorodite	$Fe^{II}AsO_4 \cdot 2H_2O$
16. Parasymplesite	$Fe^{II}_3(AsO_4)_2 \cdot 8H_2O$
17. Vivianite	$Fe^{II}_3(PO_4)_2 \cdot 8H_2O$
18. Angelellite	$Fe^{III}_4(AsO_4)_2O_3$
19. Chlorite[a]	$(Mg_{5.5}Fe^{II}_3Fe^{III}Al_{2.5})[Si_5Al_{2.5}O_{20}](OH)_{16}$

Previously published: [a] O'Day et al., 2004; [b] Root et al., 2009; [c] Hayes et al., 2009

SM Table 4: Thermodynamic constants and mode conditions for Eh pH diagram

Iron solid	log K
Jarosite $[Fe_3(SO_4)_2(OH)_6]$	9.37 [a]
$3Fe^{3+} + 2SO_4^{2-} + K^+ + 6H_2O \leftrightarrow Fe_3(SO_4)_2(OH)_6 + 6H^+$	
Schwertmannite $[Fe_8O_8(OH)_{4.8}(SO_4)_{1.6}]$	17.4 [b]
$8Fe^{3+} + 12.8H_2O + 1.6SO_4^{2-} \leftrightarrow Fe_8O_8(OH)_{4.8}(SO_4)_{1.6} + 20.8H^+$	
Ferrihydrite $[Fe(OH)_3]$	
$Fe^{3+} + H_2O \leftrightarrow Fe(OH)_3 + 3H^+$	-3.0 [c]
$Fe^{3+} + H_2O \leftrightarrow Fe(OH)_3 + 3H^+$	-5.56 [a]
Pyrite $[FeS_2]$	-24.65 [a,d]
$Fe^{2+} + 0.25SO_4^{2-} + 1.75HS^- + 0.25H^+ \leftrightarrow FeS_2 + H_2O$	

[a] Delaney and Lundeen, 1990; [b] Bigham et al., 1996; [c] Majzlan et al, 2004; [d] Lundeen, 1990

SM Figure Captions

SM Figure 1. Petrographic images of all samples. Images from reflected light, cross polarized light and x-ray fluorescence (13000 & 13050eV) from 30 μm thin sections for each depth (A-G) from the IK mine tailings.

SM Figure 2. Additional information for as-collected samples. Isolated grains were examined based on color and morphology. Panels A-C show the three distinct aggregates observed in the surface tailings, identified as Tan, Maroon and Blue. The tailings pile observed from the buildings labeled in Fig. 1 with a view to the west toward the pit on top of the pile. Panel D shows the color changes observed in the fresh pit.

SM Figure 3. Reference minerals used in S XANES linear combination fits

SM Figure 4. Reference minerals used in Fe XANES linear combination fits. Red spectra labels indicate spectra that have been published previously (Hayes et al., 2009; O'Day et al., 2004).

SM Figure 5. First-derivative Fe- XANES fits for SSE samples.

References to Electronic Annex

Bigham J. M., Schwertmann U., Carlson L., Murad E. (1990) A Poorly Crystallized Oxyhydroxysulfate of Iron Formed by Bacterial Oxidation of Fe(ii) in Acid-Mine Waters. *Geochim. Cosmochim. Acta* **54**, 2743-2758.

Bigham JM, Schwertmann U, Traina SJ, Winland RL, Wolf M. (1996) Schwertmannite and the chemical modeling of iron in acid sulfate waters. *Geochim. Cosmochim. Acta* **60,** 2111-2121.

Caraballo M. A., Rotting T. S., Nieto J. M., Ayora C. (2009) Sequential extraction and DXRD applicability to poorly crystalline Fe- and Al-phase characterization from an acid mine water passive remediation system. *Am. Mineral.* **94**, 1029-1038.

Delany J. M., Lundeen S. R. (1990) The LLNL Thermochemical Database. Reportt UCRL-21658. Lawrence Livermore National Laboratory

Dold B. (2003) Speciation of the most soluble phases in a sequential extraction procedure adapted for geochemical studies of copper sulfide mine waste. *J. Geochem. Explor*. **80**, 55-68.

Gao X., Root R., Farrell J., Ela W., Chorover J. (2013) Effect of silicic acid on arsenate and arsenite retention mechanisms on 6-L ferrihydrite: A spectroscopic and batch adsorption approach. *Appl. Geochem*. **38**, 110-120.

Hayes S. M., White S. A., Thompson T. L., Maier R. M., Chorover J. (2009) Changes in lead and zinc lability during weathering-induced acidification of desert mine tailings: Coupling chemical and micro-scale analyses. *Appl. Geochem*. **24**, 2234-2245.

Janney, D. E., Cowley, J. M., Buseck, P. R. (2000) Transmission electron microscopy of synthetic 2-and 6-line ferrihydrite. *Clays Clay Miner*. **48**, 111-119.

Majzlan J, Navrotsky A, Schwertmann U. (2004) Thermodynamics of iron oxides. III - Enthalpies of formation oand stability of ferrihydrite ($Fe(OH)_3$), schwertmannite ($FeO(OH)_{3/4}(SO4)_{i/8}$), and Fe_2O_3. *Geochim. Cosmochim. Acta* **68,** 1049-1059.

Manceau A., Gates W. P. (1997) Surface structural model for ferrihydrite. *Clay Clay Miner.* **45**, 448-460.

Michel F. M., Ehm L., Antao S. M., Lee P. L., Chupas P. J., Liu G., Strongin D. R., Schoonen M. a. A., Phillips B. L., Parise J. B. (2007) The structure of ferrihydrite, a nanocrystalline material. *Science* **316**, 1726-1729.

Neaman A, Mouele F, Trolard F, Bourrie G. (2004) Improved methods for selective dissolution of Mn oxides: applications for studying trace element associations. *Appl. Geochem*. **19,** 973-979.

O'Day P. A., Rivera N., Root R., Carroll S. A. (2004) X-ray absorption spectroscopic study of Fe reference compounds for the analysis of natural sediments. *Am. Mineral*. **89**, 572-585.

Root R. A., Vlassopoulos D., Rivera N. A., Rafferty M. T., Andrews C., O'day P. A. (2009) Speciation and natural attenuation of arsenic and iron in a tidally influenced shallow aquifer. *Geochim. Cosmochim. Acta* **73**, 5528-5553.

Waychunas G. A., Rea B. A., Fuller C. C., Davis J. A. (1993) Surface-Chemistry of Ferrihydrite .1. EXAFS Studies of the Geometry of Coprecipitated and Adsorbed Arsenate. *Geochim. Cosmochim. Acta* **57**, 2251-2269.

Zhao J. M., Huggins F. E., Feng Z., Huffman G. P. (1994) Ferrihydrite - Surface-structure and its effects on phase transformation. *Clays Clay Miner.* **42**, 737-746.

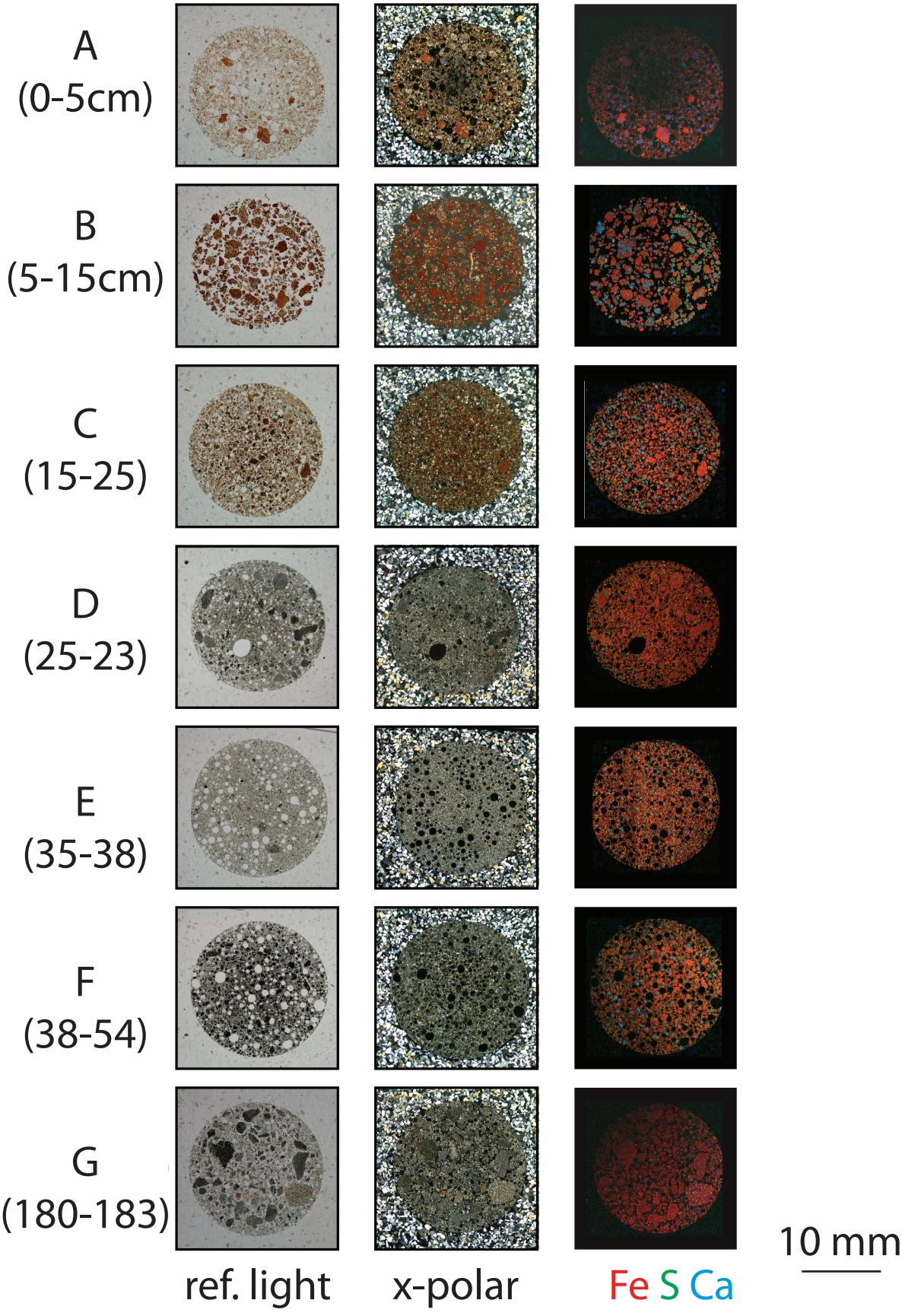
A
(0-5cm)
B
(5-15cm)
C
(15-25)
D
(25-23)
E
(35-38)
F
(38-54)
G
(180-183)
ref. light
x-polar
Fe S Ca
10 mm

Figure SM1

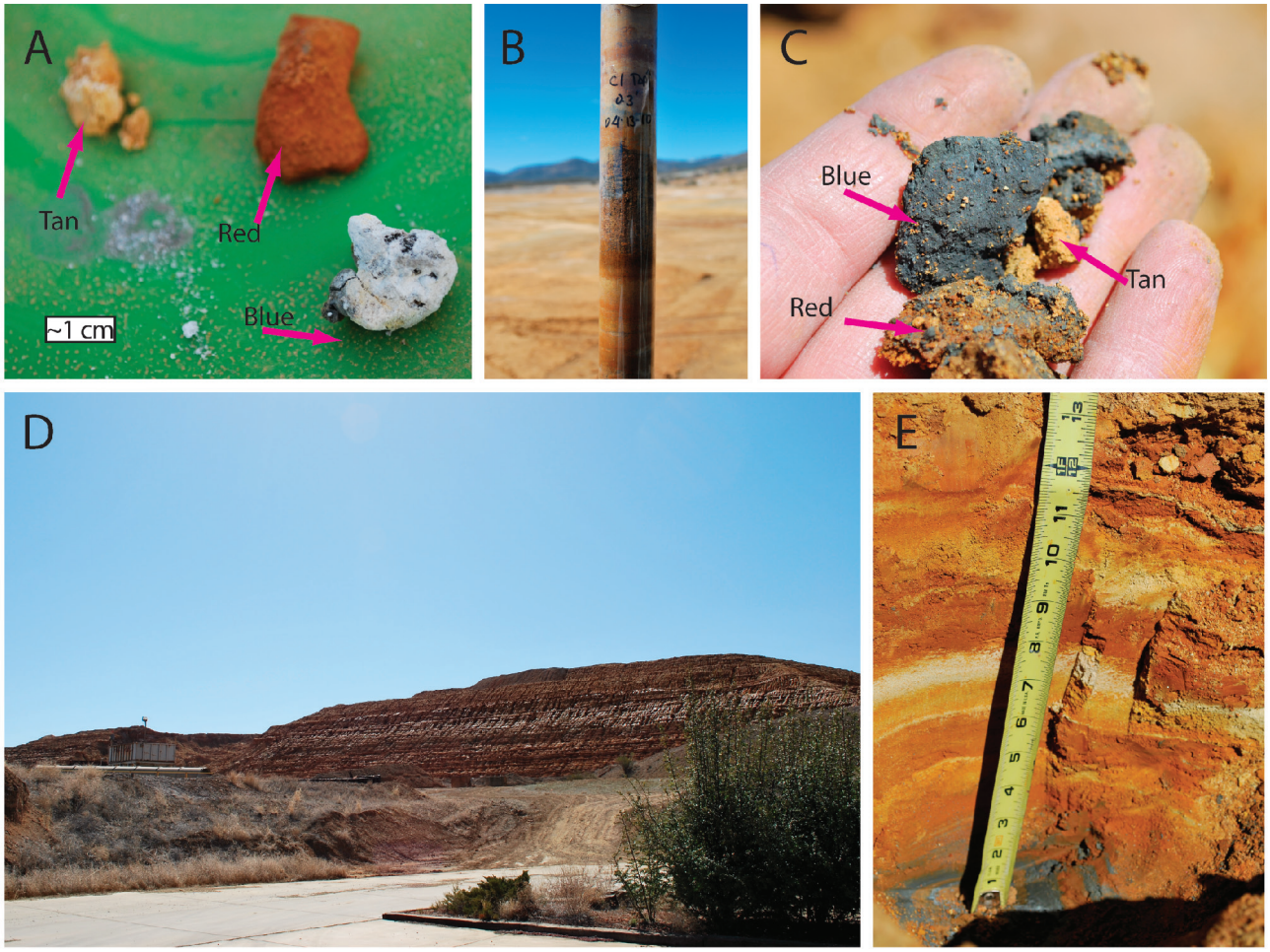

Figure SM2

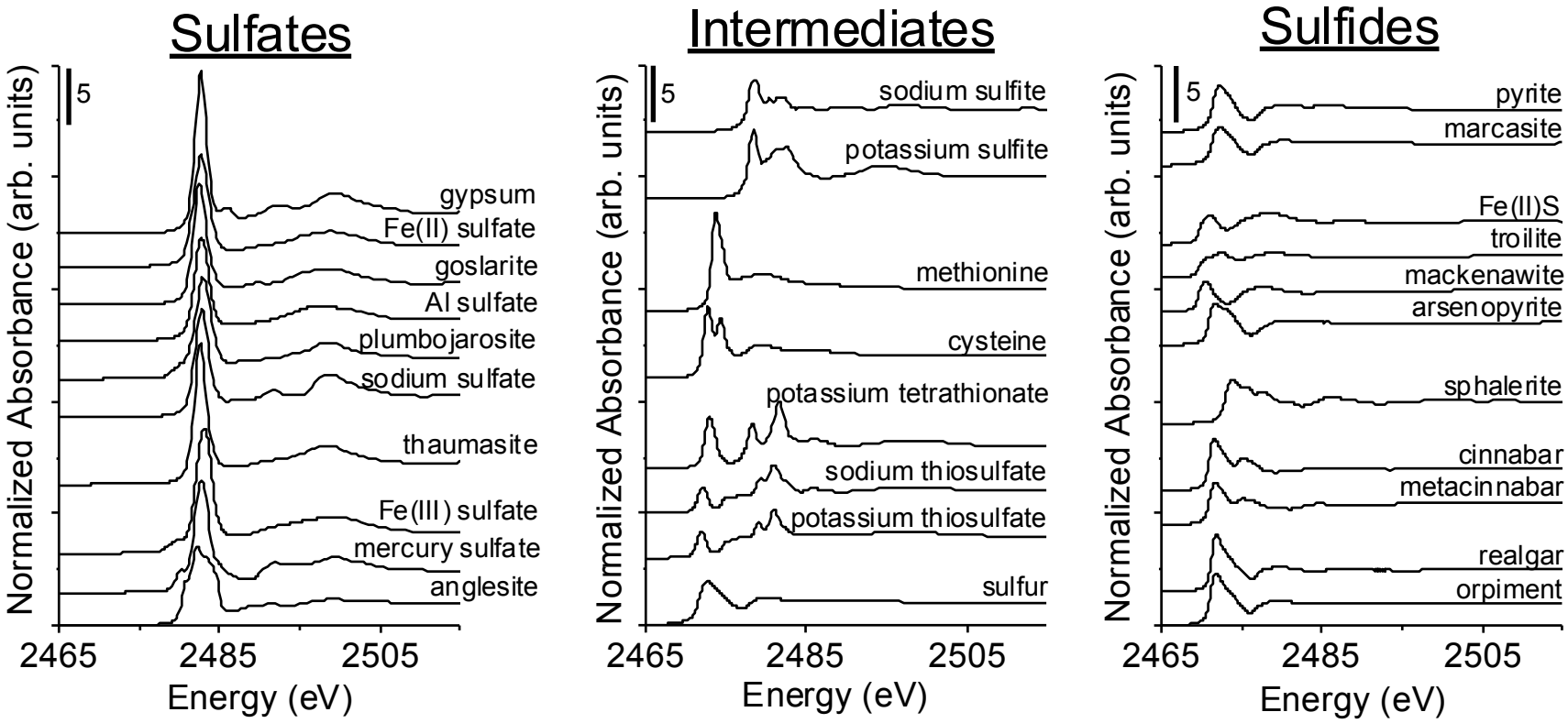
Sulfates
Intermediates
Sulfides
Normalized Absorbance (arb. units)
5
gypsum
Fe(II) sulfate
goslarite
Al sulfate
plumbojarosite
sodium sulfate
thaumasite
Fe(III) sulfate
mercury sulfate
anglesite
sodium sulfite
potassium sulfite
methionine
cysteine
potassium tetrathionate
sodium thiosulfate
potassium thiosulfate
sulfur
pyrite
marcasite
Fe(II)S
troilite
mackenawite
arsenopyrite
sphalerite
cinnabar
metacinnabar
realgar
orpiment
2465
2485
2505
Energy (eV)

SM Figure 3

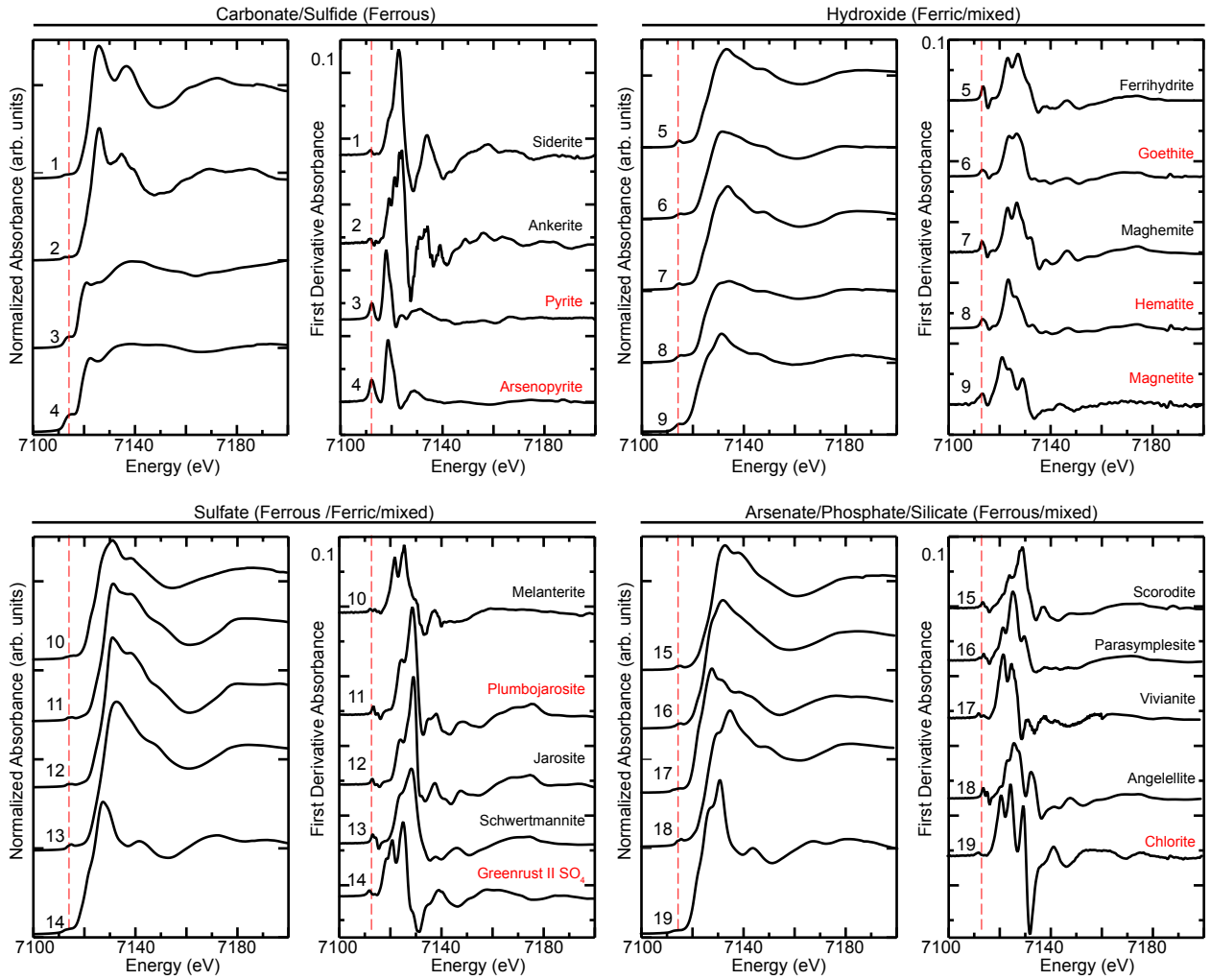
Carbonate/Sulfide (Ferrous)
Hydroxide (Ferric/mixed)
Sulfate (Ferrous /Ferric/mixed)
Arsenate/Phosphate/Silicate (Ferrous/mixed)
Normalized Absorbance (arb. units)
First Derivative Absorbance
Energy (eV)
7100
7140
7180
0.1
Siderite
Ankerite
Pyrite
Arsenopyrite
Ferrihydrite
Goethite
Maghemite
Hematite
Magnetite
Melanterite
Plumbojarosite
Jarosite
Schwertmannite
Greenrust II SO4
Scorodite
Parasymplesite
Vivianite
Angelellite
Chlorite

SM Figure 2

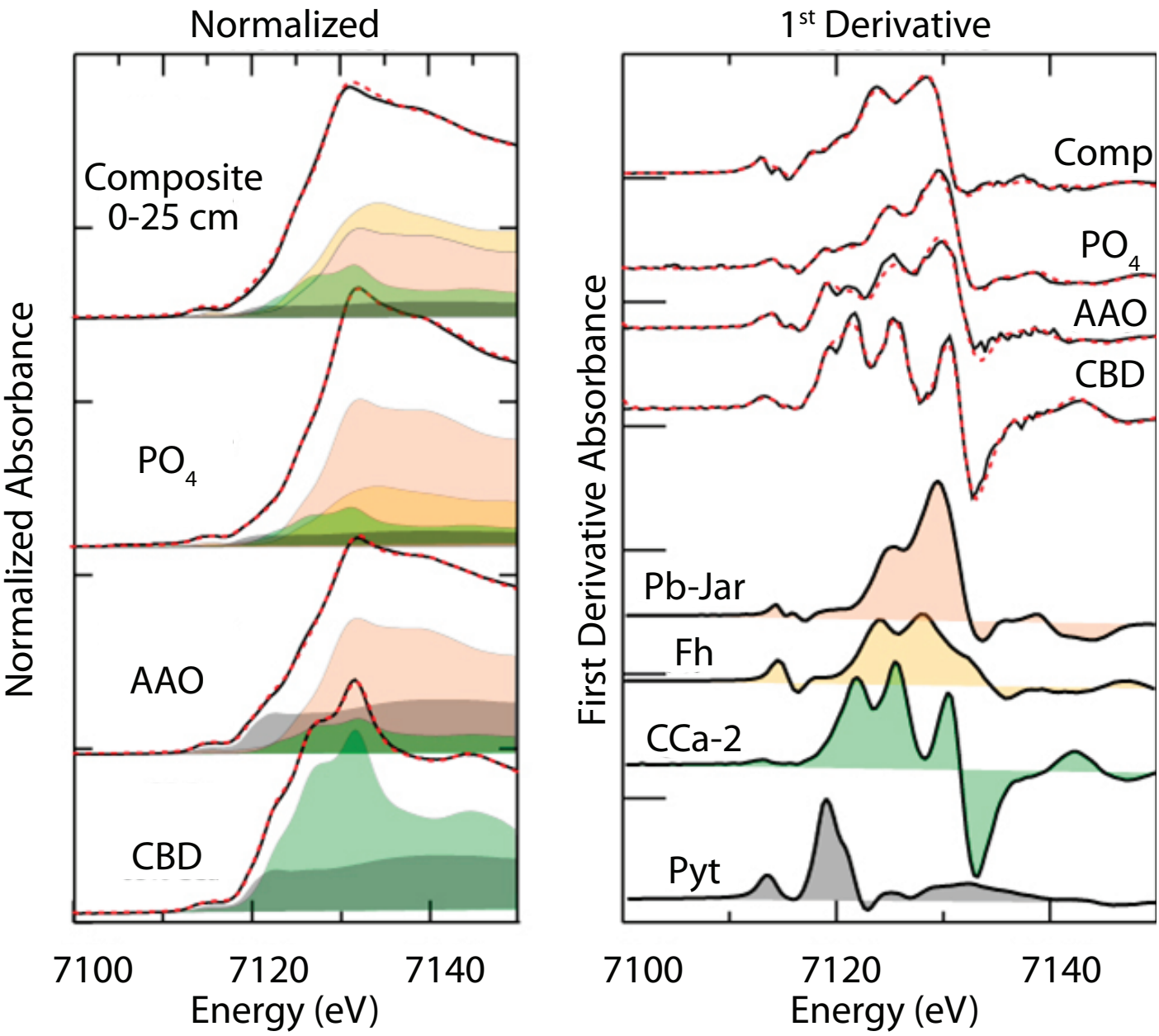
Normalized
1st Derivative
Composite
0-25 cm
PO4
AAO
CBD
Normalized Absorbance
Comp
PO4
AAO
CBD
Pb-Jar
Fh
CCa-2
Pyt
First Derivative Absorbance
7100
7120
7140
Energy (eV)
7100
7120
7140
Energy (eV)

Figure SM5